Sādhanā, Vol. 26, Parts 1 & 2, February–April 2001, pp. 139–162. © Printed in India

Modelling of convection during solidification of metal and alloys

A K SINGH, R PARDESHI and B BASU

Tata Research Development and Design Centre, 54B, Hadapsar Industrial Estate, Pune 411 013, India
e-mail: {aksingh,ravindrap,bbasu}@pune.tcs.co.in

Abstract. The role of convection during solidification is studied with the help of a mathematical model. The effect of various mush models on convection and consequent macrosegregation is examined with the help of numerical simulations. The predicted macrosegregation profiles are compared with published experimental data. Subsequently, the importance of proper auxiliary relationship for thermo-solutal coupling in the mushy region is highlighted through some careful numerical simulations. Finally, the role of material parameters on double-diffusive convection is illustrated through comparative study of solidification of aqueous ammonium chloride, iron–carbon and lead–tin binary systems. Important results of these studies are presented and discussed.

Keywords. Double-diffusive convection; solidification of metals and alloys; modelling of solidification; mushy region.

1. Introduction

Solidification is the heart of many important manufacturing processes such as casting, welding, laser processing, crystal growth etc. It is governed by a number of interacting governing phenomena like transport of energy and solute, convection, nucleation, growth etc. and properties of solidified components like segregation, structure, porosity, strength etc. are finally controlled by one or more of these phenomena (Beckermann & Viskanta 1988; Ghosh 1990). In the majority of the cases, the transition from liquid to solid takes place in the presence of convection. Some of the common causes of natural convection are (1) thermal buoyancy, (2) solutal buoyancy, (3) shrinkage etc. The flow can also be induced by means of external forces. The methods commonly employed to generate convection in the melt are (a) electromagnetic stirring, (b) mechanical stirring, rotation etc.

Flow during solidification affects the properties of the solidified products significantly. Some of these effects are listed below:

A list of symbols is given at the end of the paper

(1) Morphology of solid/liquid interface: Flow plays an important role in the transition from planar-to-cellular and cellular-to-dendrite interface.
(2) Microstructure: Flow affects the evolving microstructure through changes in cooling rate and solute concentration.
(3) Macrostructure: Flow has major effect on morphology and morphological transition (columnar-to-equiaxed transition, for example).
(4) Segregation: Macrosegregation is widely attributed to the convection in the mushy and superheated regions. It is also influenced by the morphological transition, which, in turn, is influenced by flow.
(5) Microsegregation: It is caused primarily by diffusion. However, since both morphology and solute concentration are affected by flow, microsegregation is influenced by it as well.
(6) Freckles: This defect is attributed to the plumes of solute-rich liquid emanating from channels in the mushy region.

Effects of flow during solidification have been observed through experiments on transparent systems. Thompson & Szekely (1988) have reported experimental observations on solidifying aqueous sodium carbonate where the vertical nature of the solid–liquid interface in a horizontal solidification could be seen altered under the influence of flow. Similarly, several researchers have carried out experimental and numerical study on solidification of aqueous ammonium chloride solutions (Beckermann & Viskanta 1988; Worster 1997). The above cases are examples of double-diffusive convection during progress of solidification.

Double-diffusive convection effect during solidification has been extensively studied in the past. Basu & Singh (1997) present an overview of literature on double-diffusive convection as well as a continuum formulation based mathematical model. As discussed there, one of the central features of the mathematical modelling of convection is the representation of the mushy region and both isotropic and anisotropic models of permeability have been used in the past. It is important to note that experimental data on permeability are limited to the middle portion of the mushy region. Several attempts have been made in the past to circumvent this difficulty. Recently, Goyeau *et al* (1999) have evaluated permeability tensor form digitized images by use of the classical closure problem. Some very promising results are obtained. This remains a key area as far as predictive power of the model of convection is concerned.

Effects of various parameters affecting double-diffusive convection and macrosegregation are reported in this paper. The mathematical model used in this study is described in the next section. The role of mush model on macrosegregation is examined through simulations with various mush models and comparison of model predictions with experimental data and other numerical results. Apart from the role of appropriate mush model, there are other modelling issues, which require close attention. Subsequently the role of auxiliary relationship for thermo-solutal coupling in the mushy region is examined with the help of few careful simulations. Finally, the role of material parameters on double-diffusive convection during solidification of binary alloys is investigated through comparative study of solidification of three binary alloys, namely, aqueous ammonium chloride, Fe–C and Pb–Sn.

2. Mathematical model

2.1 *Governing equations*

In the present study, a mass average based continuum formulation (Bennon & Incropera 1987) is used in the development of the model. The following simplifying assumptions are invoked in the development of the present model.

(a) Solidification proceeds in columnar fashion and Darcy's law is applicable to describe flow in the mushy region;
(b) Boussinesq assumption is invoked for density variation;
(c) local thermal equilibrium exists between solid and liquid phases; and
(d) flow is laminar and is well represented by a 2-D model.

Governing equations for this model are based on convection of mass, momentum energy and solute and are listed in table 1. The sets of governing equations along with the auxiliary relationship (Bennon & Incropera 1987) are solved using finite volume method (Patankar 1980). The geometry of the rectangular cavity is shown in figure 1. The melt was initially isothermal, chemically homogeneous, and quiescent. No-slip velocity conditions were imposed at the walls, which were impermeable to all species. In the numerical experiment, solidification was initiated by imposing a convective heat flux ($q = U\,[T_s - T_c]$) from the right vertical wall of the rectangular cavity. All other boundaries were assumed adiabatic.

Table 1. Continuum conservation equations and descriptions of relevant continuum parameters.

Continuity:	$\frac{\partial}{\partial t}(\rho) + \nabla\cdot(\rho V_m) = 0$
x-momentum:	$\frac{\partial}{\partial t}(\rho u_m) + \nabla\cdot(\rho V_m u_m) = \nabla\cdot\left(\mu_l \frac{\rho}{\rho_l}\nabla u_m\right) + \rho B_x - \frac{\mu_l}{K}\frac{\rho}{\rho_l}(u_m - u_s) - \frac{\partial P}{\partial x}$
y-momentum:	$\frac{\partial}{\partial t}(\rho v_m) + \nabla\cdot(\rho V_m v_m) = \nabla\cdot\left(\mu_l \frac{\rho}{\rho_l}\nabla v_m\right) + \rho B_y - \frac{\mu_l}{K}\frac{\rho}{\rho_l}(v_m - v_s) - \frac{\partial P}{\partial y}$
Energy:	$\frac{\partial}{\partial t}(\rho h) + \nabla\cdot(\rho V_m h) = \nabla\cdot\left(\frac{k}{c_s}\nabla h\right) - \nabla\cdot[(h_l - h)(u_m - u_s)]$
Species:	$\frac{\partial}{\partial t}(\rho f^a) + \nabla\cdot(\rho V_m f^a) = \nabla\cdot\left(\rho D\nabla f^a\right) - \nabla\cdot\left[\rho D\nabla(f_l^{\,a} - f^a)\right] - \nabla\cdot\left[\rho(f_l^{\,a} - f^a)(V_m - V_s)\right]$
Dependent continuum variable:	$f_m = g_s f_s + g_l f_l$
Continuum density:	$\rho_m = g_s \rho_s + g_l \rho_l$
Continuum thermal conductivity:	$k_m = g_s k_s + g_l k_l$
Continuum mass diffusion coefficient:	$D_m = g_l D_l$
Permeability:	$K_s = K_0[g_l^3/(1-g_l)^2]$

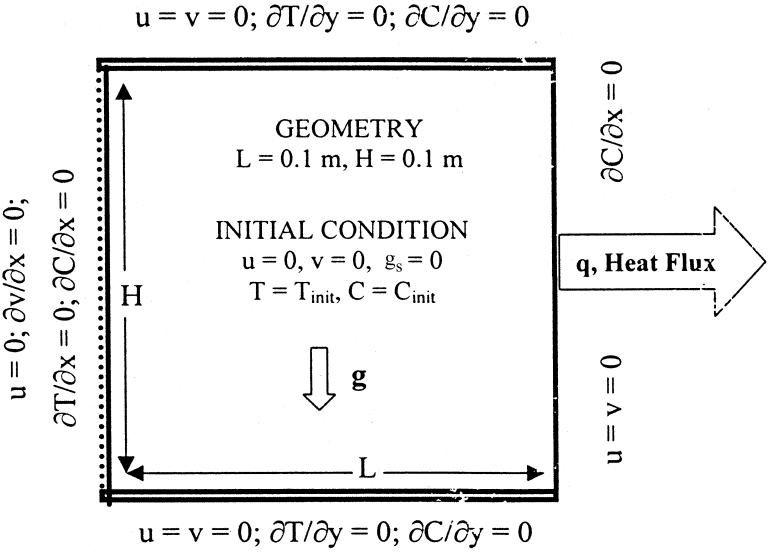

Figure 1. Geometry of the cavity and initial and boundary conditions.

3. Role of mush models on convection and macrosegregation

3.1 *Problem definition*

As mentioned earlier, the model was used to simulate the experiments carried out by Krane & Incropera (1997). The melt chosen was a binary Pb–40 wt% Sn alloy with an initial temperature of 239°C. The rectangular cavity, which was 89 mm wide and 75 mm tall, was filled with molten alloy. Thermophysical properties for this system are listed in table 2. Heat transfer coefficient was taken to be 35 W/m^{2}K (Krane & Incropera 1997).

The model, described in §2, was used to examine the role of permeability correlation on macrosegregation during solidification of a binary alloy. The most commonly used expression for representing the permeability function is the Blake–Kozeny correlation (Brinkman 1947), which is represented as:

$$K = K_0(g_l^3/(1-g_l)^2), \tag{1}$$

where K is the permeability of the mushy region, used in the Darcy term of momentum equations (table 1). The permeability coefficient, K_0, in the Blake–Kozeny model, (1), is dependent on microstructural details, namely, primary and secondary dendrite arms spacing. Krane & Incropera (1997) have used the following expression, given by Asai & Muchi (1978), for evaluation of permeability constant, K_0 (m^2):

$$K_0 = d^2/180, \tag{2}$$

where d is the dendrite arms spacing in *m*m.

Table 2. Thermophysical properties.

	$NH_4Cl–H_2O$	Fe–C	Pb–Sn
Initial T (C)	295·0	1463·0	276·0
Initial ΔT (C)	5·0	5·0	5·0
Initial C (wt%)	18·0	1·0	15·0
Cavity size (m)	$0{\cdot}1 \times 0{\cdot}1$	$0{\cdot}1 \times 0{\cdot}1$	$0{\cdot}1 \times 0{\cdot}1$
r (kg/m^3)	1000·0	6940·0	10600
C_p (S) (J/kgK)	3000·0	753·0	148·0
C_p (L) (J/kgK)	3000·0	753·0	172·0
k (S) (W/mK)	0·4	60·0	38·2
k (L) (W/mK)	0·4	30·0	21·25
b_T (1/K)	-3.83×10^{-4}	$-2{\cdot}7 \times 10^{-4}$	$-1{\cdot}09 \times 10^{-4}$
b_C	–0·26	–0·686	–0·364
m (kg/ms)	$1{\cdot}0 \times 10^{-3}$	$6{\cdot}94 \times 10^{-3}$	$2{\cdot}31 \times 10^{-3}$
ΔH (J/kg)	$3{\cdot}0 \times 10^{5}$	$2{\cdot}72 \times 10^{5}$	$2{\cdot}84 \times 10^{4}$
Eutectic T (°C)	–15·4	1130·0	183·0
Eutectic C (wt%)	80·3	4·3	61·9
K_o (m^2)	$5{\cdot}0 \times 10^{-10}$	$2{\cdot}8 \times 10^{-11}$	$2{\cdot}8 \times 10^{-11}$
Melting point (°C)	357·0	1536·0	327·0
D (S) (m^2/s)	$4{\cdot}8 \times 10^{-12}$	$4{\cdot}8 \times 10^{-12}$	$4{\cdot}8 \times 10^{-12}$
D (L) (m^2/s)	$4{\cdot}8 \times 10^{-9}$	$1{\cdot}0 \times 10^{-9}$	$1{\cdot}5 \times 10^{-9}$

Using typical dendrite arm spacing of the order of 100 mm (Krane & Incropera 1997), gives K_0 of the order of 10^{-10} m^2. Predicted macrosegregation, using the above value of permeability coefficient, was found to be on higher side (Krane & Incropera 1997). In fact, the permeability value, which provides proper fit to the macrosegregation data, is of the order of 10^{-11} m^2, which is an order of magnitude less than the calculated value. It is useful to recall that the Blake–Kozeny expression provides isotropic permeability. In order to examine the effect of this simplifying assumption, simulation studies were carried with both isotropic and anisotropic mush models. Comparison of various mush models, in two orthogonal directions, i.e., flow parallel to primary dendrite arm spacing and flow perpendicular to primary dendrite arm spacing, is presented by Poirier (1987).

Of various models describing flow parallel to dendrites, Poirier (1987) found that the multi-linear regression-based model and the Hagen–Poiseuille model gave almost identical results. Since the Hagen–Poiseuille model had a physical basis, this correlation was used to describe the flow parallel to the dendrites. This model is tested for liquid fraction in the range of 0·17 to 0·61. Beyond this range, Poirier recommended use of Blake–Kozeny model. Thus, for g_l less than 0·17 and greater than 0·61, Blake–Kozeny model was used with some modifications (K_0 is modified in such a way to provide continuity in K at g_l equal to 0·17 and 0·61).

For flow perpendicular to the dendrites, Poirier (1987) recommended use of a multi-linear regression based model for g_l between 0·19 and 0·66 (permeability data are available

within these boundaries only). Beyond this range, the Blake–Kozeny expression was recommended for the permeability value.

Thus, for the present simulation study, the following mush models and permeability coefficient were used.

Case I: Isotropic Blake–Kozeny model for all g_l with $K_0 = 2{\cdot}8 \times 10^{-11}$ m^2.

Case II: Isotropic Blake–Kozeny model for all g_l with $K_0 = 2{\cdot}8 \times 10^{-10}$ m^2.

Case III: Poirier anisotropic model.

For flow parallel to dendrite arm:

For $g_l > 0{\cdot}61$,	Blake–Kozeny, $K_0 = 1{\cdot}2 \times 10^{-11}$ m^2,
For $g_l > 0{\cdot}17$ and $< 0{\cdot}61$,	Hagen–Poisseulle, $K = 3{\cdot}75 \times 10^{-12}\, g^2{}_l$ m^2,
For $g_l < 0{\cdot}17$,	Blake–Kozeny, $K_0 = 1{\cdot}0 \times 10^{-12}$ m^2.

For flow perpendicular to dendrite arm:

For $g_l > 0{\cdot}66$,	Blake–Kozeny, $K_0 = 4{\cdot}6 \times 0^{-12}$ m^2
For $g_l > 0{\cdot}19$ and $<0{\cdot}66$,	multi-linear regression
	$K = 1{\cdot}0 \times 10^{-3}\, g_l^{3{\cdot}32} d^{2{\cdot}08} = 4{\cdot}7 \times 10^{-12}\, g_l^{3{\cdot}32}$ m^2,
For $g_l < 0{\cdot}19$,	Blake–Kozeny $K_0 = 1{\cdot}3 \times 10^{-12}$ m^2.

In all the above expressions, the value of d is taken as 100 mm.

3.2 *Results and discussion*

Figure 2 shows the double-diffusive convection pattern at various times during the progress of solidification, i.e., for case I, where the Blake–Kozeny model with $K_0 = 2{\cdot}8 \times 10^{-11}$ is used at all liquid fractions. The flow pattern depicts the reversal of convective pattern with progress of solidification. At 250 s, the thermal cell has completely dissipated due to extinction of the melt superheat, and the solutal cell, which is weak, dominates the flow. It shows tin-rich segregates and strip at the top. Due to flow reversal, solute rejected during solidification is carried to the top of the mold. This leads to a positive macrosegregation at the top and a negative macrosegregation at the bottom of the cavity. The calculated extent of the tin-rich band along the top of the ingot increases with increase in permeability. Although the detailed flow pattern and final macrosegregation for other cases are not shown for lack of space, it is noted that the flow reversal takes place in all three cases.

Numerical predictions of final macrosegregation for all three cases are shown in figures 3a–d. It is readily noticed that these differ from each other both qualitatively as well as quantitatively. Figure 3a shows the composition in a vertical section at $x = 19$ mm. Good agreements are seen for both case I and case III. On the other hand, the Blake–Kozeny model of case II, where permeability coefficient is calculated from the Asai & Muchi (1978) correlation, results in over-prediction of macrosegregation. Again the same trend is visible in figures 3b and 3c. It is seen that the match between measurement and prediction

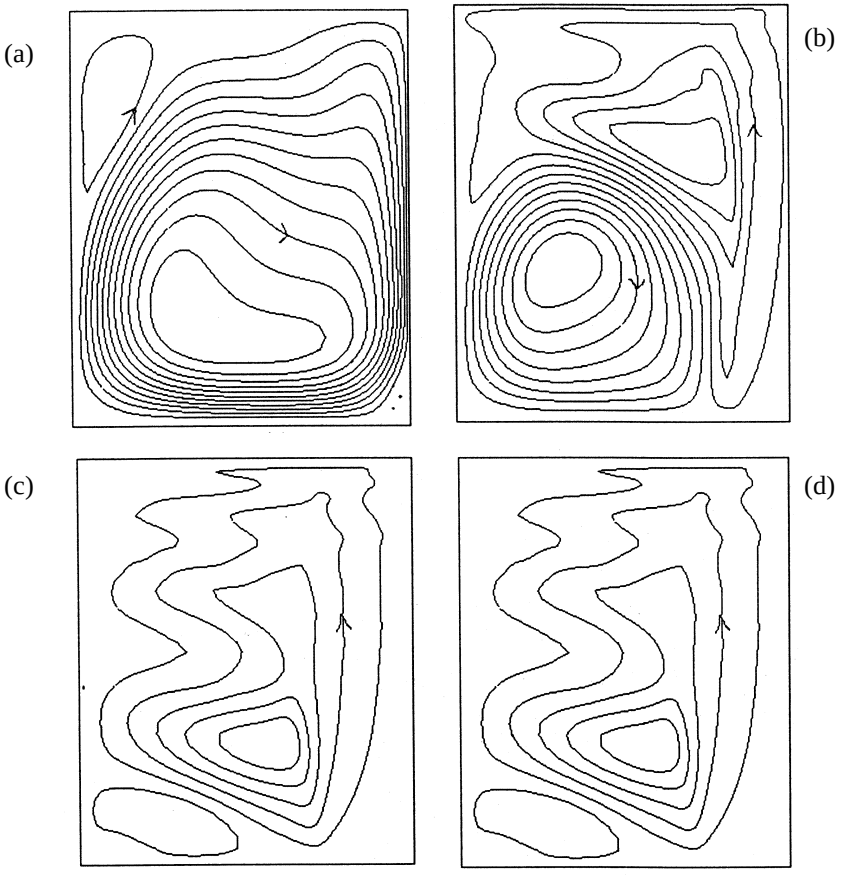

Figure 2. Streamline plots after (**a**) 30 s (max = 0·1092, min = –0·9977), (**b**) 60 s (max = 0·7183, min = –0·3735), (**c**) 90 s (max = 0·3569, min = – 0·5696), and (**d**) 120 s (max = 0·2306, min = – 0·0462).

is good for both cases I and III at these two horizontal sections of the casting. In contrast, case II, where $K_0 = 2{\cdot}8 \times 10^{-10}$ is used, shows large deviations.

Finally, figure 3d shows spikes in the predicted composition profiles near the chilled wall ($x < 25$ mm) in all the cases, which is not present in the measurement. This could be due to scarcity of permeability data in the mushy region close to the liquidus.

The closeness of predictions in cases I and III is due to similar permeability values for both these cases. Thus use of the Blake–Kozeny isotropic model requires tuning of permeability coefficient by a factor of 10 (case I). In contrast, the anisotropic model gives similar results without resorting to tuning.

The comparative study described above that suggests that an improvement in predictive power of the mathematical model is possible (in some parts) through selection of a better mush model. In addition to this, the following points are found to be of importance.

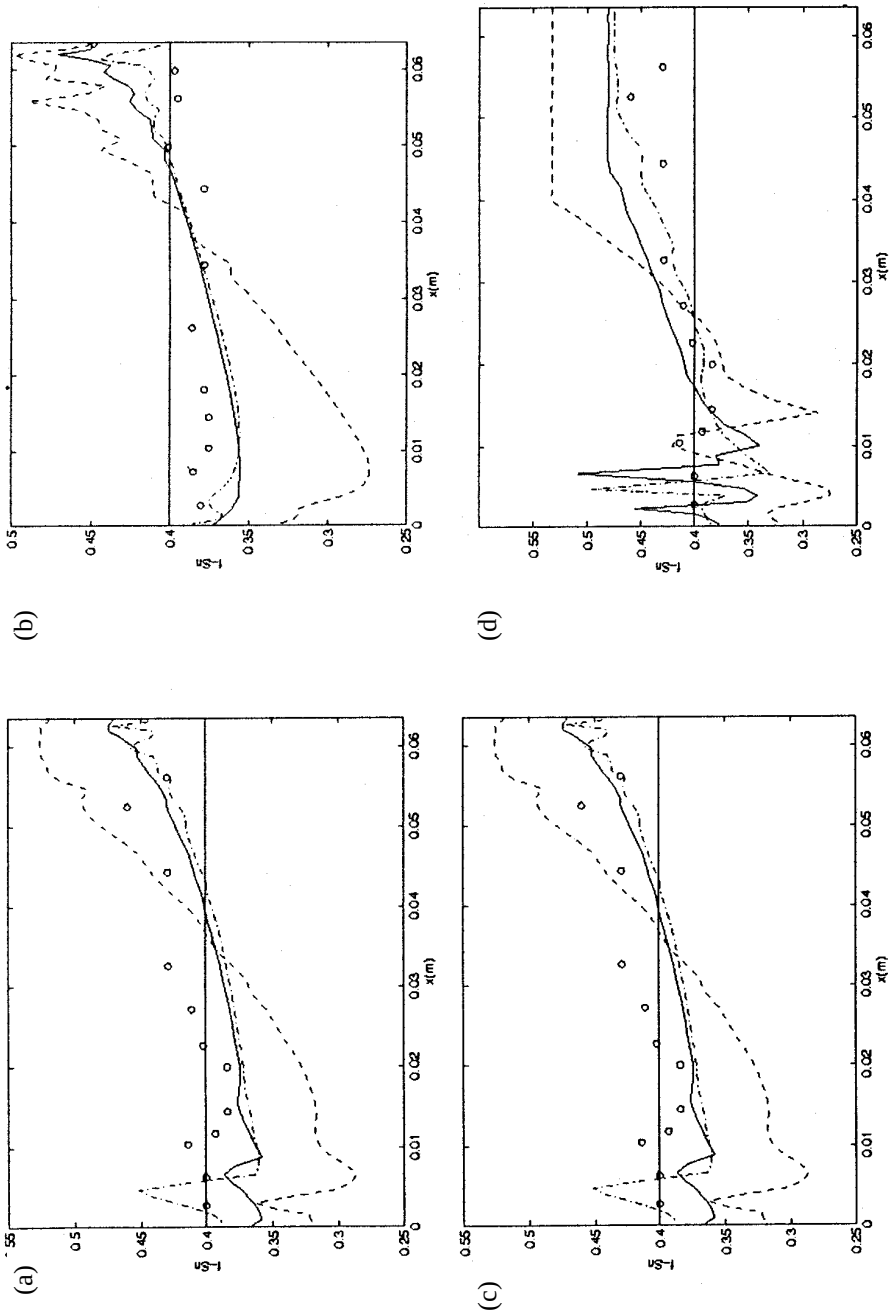

Composition profile for Pb -40% Sn: (**a**) x = 19 mm; (**b**) y = 15 mm; (**c**) y = 39 mm; (**d**) y = 69 mm. The -axis denotes distance from the cold wall. —— Blake–Kozeny model w ith $K_0 = 2{\cdot}8 \times 10^{-11}$; -- model based on --- Blake–Kozeny model with $K_0 = 2{\cdot}8 \times 10^{-10}$; O experimental data (Bennon & Incropera 1988).

- The permeability coefficient of the isotropic Blake–Kozeny model, based on the geometry of primary dendrite arms, requires substantial modification for representing experimental data on macrosegregation.
- Anisotropic model shows better match with experimental data.
- For further improvements in predictive power, better mush models are required for g_1 between 0·7 and 1·0.

4. Role of appropriate auxiliary relationship on convection

4.1 *Problem definition*

This example examines the role of proper auxiliary relationship on convection during solidification. These cases are discussed in detail in recent work by Singh & Basu (2000). The role of thermo-solutal buoyancy forces on the flow and of thermo-solutal coupling on the permeability of the porous network and, in turn, on the flow in the mushy phase, are studied with the help of the model described in §2. In this exercise, the value of permeability is calculated based on the correlation given by West (1985) with suitable modifications to account for the iron–carbon system (Singh & Basu 1997). The expressions used for permeability are presented below.

$$K = T_1 (Y_1 K_1 + T_2 Y_2 K_2) \tag{3}$$

where, $K_1 = g_l^2$, for all g_l, $K_2 = 0$, for $g_l < 1/3$ and $K_2 = g_s^{2/3}[3 + 4/g_s – 3x(8/g_s – 3)^{0·5}]$, for $g_l > 1/3$, $Y_1 = 6·4 \times 10^{-13}$ m^2; $Y_2 = 8·8 \times 10^{-11}$ m^2; $T_1 = 137·5$ and $T_2 = 0·5\ g_l/g_s$.

It is seen from (3) that the permeability correlation is dependent on the local liquid fraction. Local liquid fraction in the mushy region is dependent on the thermo-solutal coupling, which is mainly governed by the solidification conditions. There are several equations to represent this relationship. In case of slow solidification and/or interstitial solute, the process can be considered to be close to equilibrium. In such cases, the temperature and the solute concentration in the mushy region are related to the local liquid fraction through the phase diagram. The resultant Lever rule is shown below.

$$g_l(T,C) = \frac{[mC - k(T - T_f)]}{[(1-k)(T - T_f)]}, \tag{4}$$

where, g_l is local liquid fraction, T_f is fusion temperature of pure component, k is partition coefficient and m is slope of the liquidus.

Rapid solidification processes (Kurz & Fisher 1992) are at the other extreme; here the temperature and the solute concentration in the mushy region may be independent of each other as in the case of non-equilibrium solidification. The progress of solidification in such cases could be dependent on the temperature alone. A relationship between g_l–T, used sometimes in conduction dominated solidification is shown below.

$$g_l(T, C) = (T_l - T)/(T_l - T_s), \tag{5}$$

where, T_s and T_l are the liquidus and solidus respectively.

In between these two extreme cases, there lies a host of possibilities. The Scheil equation (Scheil 1942), which assumes no back-diffusion in the solid and complete mixing in the liquid, falls in this category. For the sake of completeness, the, well-known Scheil equation is presented below,

$$g_l(T, C) = [(T - T_f)/(T_l - T_f)]^{1/(k-1)}. \tag{6}$$

Temperature at the solid–liquid interface is in local equilibrium in this case. However, the temperature and the solute behind the interface are not coupled through the equilibrium equation. The above equations, i.e., (4) to (6), are very important for models determining flow through the mushy region and consequent macrosegregation.

Thermal and solutal fields not only determine drag in the mushy region but are also responsible for the flow (through buoyancy forces). In the present study, the Boussinesq approximation is invoked. Therefore, the density of both solid and liquid are assumed constant except in the buoyancy expression. The following linear expression is used for variation of density in the buoyancy term,

$$r_{\text{eff}} = r[b_T(T - T_{\text{ref}}) + b_C(C - C_{\text{ref}})]. \tag{7}$$

From the above discussion it is clear that thermal and solutal fields affect flow and macrosegregation through their effects on both drag and buoyancy terms. For the purpose of this study, solidification is considered in a rectangular cavity of length 100 mm and height 100 mm. The boundary conditions are as follows: no-slip conditions are applied on the horizontal and the vertical walls of the cavity. The left vertical wall of the cavity is the line of symmetry. Thus, the gradient of v-velocity along the x-axis, i.e., $\partial v/\partial x$, is zero along the left wall of the cavity. Similarly, the solute fluxes are zero at all four boundaries of the cavity. As for thermal boundary conditions, the horizontal walls of the cavity are adiabatic and there is no heat flux at the left wall. The right vertical wall is used for heat extraction.

The material chosen for the present study is Fe–1 wt% C; the liquidus and the solidus temperatures for this composition are 1458 and 1375°C respectively. All simulation studies are carried out with an initial melt temperature of 1463°C. Solidification is initiated by imposing a heat flux of 60 kW/m^2 from the right vertical wall of the cavity. The following three case studies are simulated:

Case 1 is based on the complete set of transport equations; it incorporates the effect of double-diffusive convection. In this case, the solutal field is coupled with temperature in the mushy region through the Lever rule, (4). Therefore, it contributes to the flow field in two ways: (1) through *convection generating forces*, and (2) through *its effect on resistance to the flow*.

Case 2 is a study of macrosegregation based on thermal buoyancy driven flow, i.e., by neglecting the solutal buoyancy term in (7). However, the thermal and the solutal fields are coupled by the Lever rule as in case 1, (4). The solutal field, in this case, will control the flow field through the *resistance of the mushy phase only*. The specific role of solutal buoyancy on macrosegregation will be established from this study.

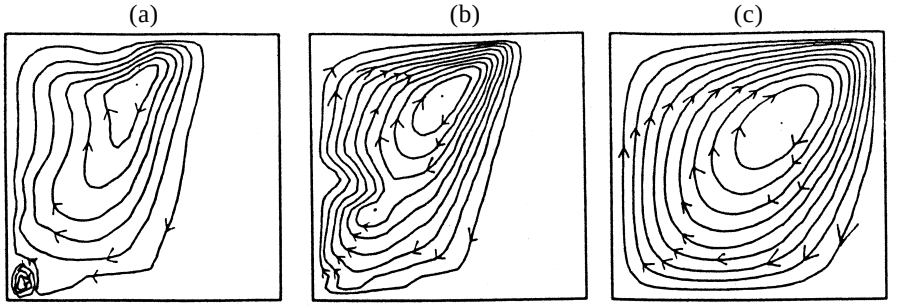

Figure 4. Predicted streamlines (equal increments) at 1300 s. (**a**) Case 1 – max 3·6, min –1·9. (**b**) Case 2 – max 3·8, min –0·1. (**c**) Case 3 – max 7·7, min –0·1.

Case 3 is based on thermal buoyancy driven flow with linear latent heat release in the mushy phase, i.e., the mushy phase is dependent on the temperature field only, (5). In this study, the solutal field makes *no contribution* to the flow field.

4.2 *Results*

The results of these case studies are presented below. Figure 4 shows the flow field in the form of streamlines after a lapse of 1300 s from the beginning of heat extraction from the right vertical wall of the cavity. The respective isotherms, solid fraction profiles and macrosegregation profiles are shown in figures 5–7. It can be seen that the flow field with double-diffusion convection (case 1) is relatively more complex in nature as compared to case 2. The similarities between these two cases are due to the dominance of thermal buoyancy over solutal buoyancy in iron–carbon alloy (Basu & Singh 1997) and also due to the usage of similar thermo-solutal coupling in the mushy region. On the other hand, there are differences between the two near the bottom left corner of the cavity where a reverse vortex is seen in this case. In contrast to these two cases, the flow field for case 3 shows the presence of a single large vortex due to thermal buoyancy as predicted by researchers in the past (Voller & Prakash 1987; Basu 1991). However, the flow field in this case is much stronger (see the footnote in the figure) than in the first two cases.

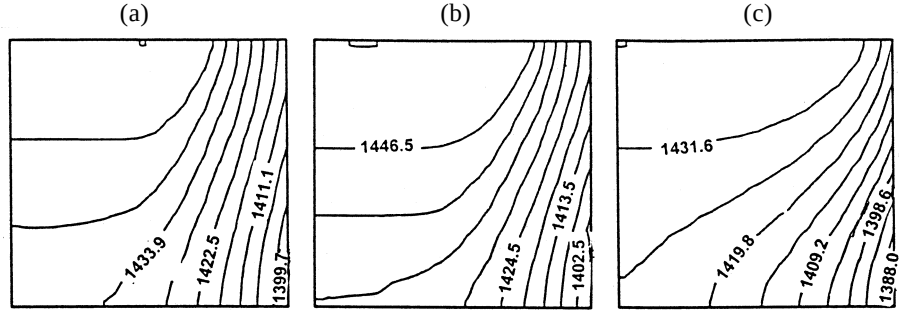

Figure 5. Predicted isotherms (equal increments) at 1300 s. (**a**) Case 1 – max 1454, min –1397°C. (**b**) Case 2 – max 1454, min 1399°C. (**c**) Case 3 – max 1438, min 1385°C.

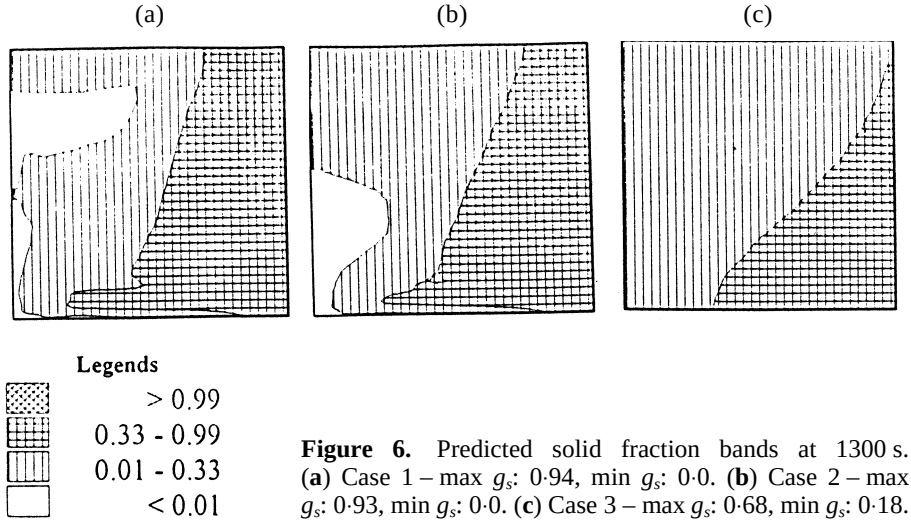

Figure 6. Predicted solid fraction bands at 1300 s. (**a**) Case 1 – max g_s: 0·94, min g_s: 0·0. (**b**) Case 2 – max g_s: 0·93, min g_s: 0·0. (**c**) Case 3 – max g_s: 0·68, min g_s: 0·18.

In order to get further insight into the flow behaviour in these cases, the isotherms and constant solid fraction contours, which signify the resistance offered by the mush, are shown in figures 5 and 6 respectively. It is seen that the isotherms of figures 5a and 5b are identical in most parts of the cavity. However, near the bottom left corner, the presence of minor vortex results in localized thermal homogenization. In addition to this, the isotherm of case 1 gets pushed up further along the hot wall due to the presence of double-diffusive convection. This point is more clearly observed in figure 6. It can be seen that the solid fraction distribution of case 2 is somewhat different from that of case 1 in the region near the hot wall. In both these cases, there is a superheated liquid domain surrounded by a

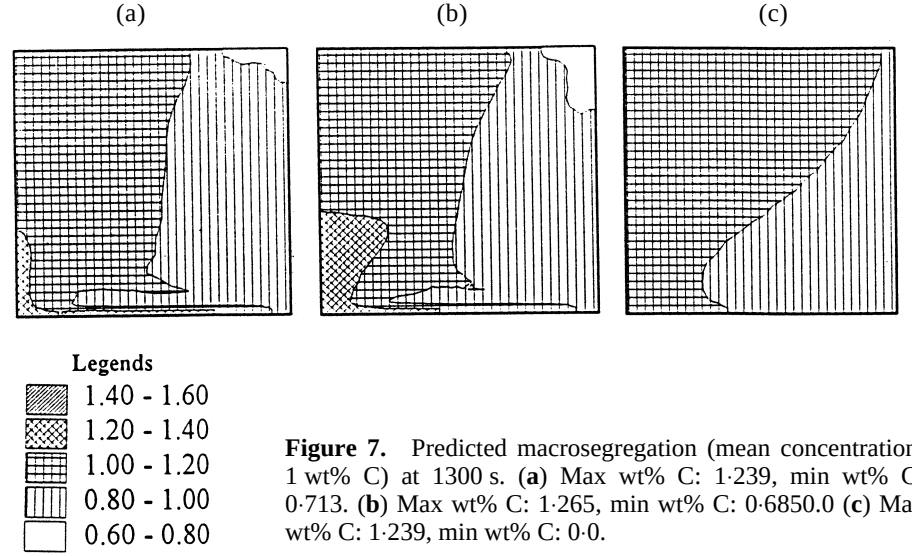

Figure 7. Predicted macrosegregation (mean concentration: 1 wt% C) at 1300 s. (**a**) Max wt% C: 1·239, min wt% C: 0·713. (**b**) Max wt% C: 1·265, min wt% C: 0·6850.0 (**c**) Max wt% C: 1·239, min wt% C: 0·0.

mushy region (shown by hatched lines). However, it is seen from figure 6b that the superheated liquid occupies the region along the bottom half of the hot wall, whereas, the same has moved up along the hot wall in case 1, figure 6a. As stated earlier, thermal and solutal buoyancies aid each other near the hot wall, which results in the above effect. The above phenomenon clearly demonstrates the role of solutal buoyancy.

As opposed to these two cases, the mush structure for case 3, shown in figure 6c, is distinctly different. The proportion of sparse mushy region ($g_s < 0{\cdot}33$) is very high in this case as mush is controlled by thermal field alone rather than the thermo-solutal coupling. This results in faster spread of mushy region. The isotherms for this case are shown in figure 5c. The maximum and the minimum temperatures in the cavity (1438°C and 1385°C respectively) are lower compared to cases 1 and 2. This is on account of better mixing of case 3.

The macrosegregation profiles, shown in figure 7 ($t = 1300$ s), indicate that similar complex solute distributions develop away from the hot wall in cases 1 and 2; however, the profile that develops in case 3 is much simpler and the magnitude of macrosegregation is not as great. Cases 1 and 2, however, differ in minute details. For example, the severity of segregation near the cold wall is less for case 1 as seen from the reduced area under the segregation band of 0·6 to 0·8. It is noted that thermal and solutal buoyancies oppose each other near the cold wall leading to reduction in the net flow strength for case 1 and consequent macrosegregation. Secondly, the zone of positive segregation near the bottom left corner of the cavity is seen to be larger in case 2 (solutal buoyancy is ignored in this case). As in the case of isotherms, the presence of double-diffusive cell near the left bottom corner of the cavity leads to localized solute homogenization in case 1.

In contrast to the complex macrosegregation patterns of cases 1 and 2, that for case 3 is simple. Thus, the absence of thermo-solutal coupling leads to a more uniform mush structure, provides less time for solute transport from the mushy region to other parts of the cavity and imparts better mixing of solute due to the high strength of the flow. These trends continue till the end of solidification.

The final macrosegregation patterns (at the end of solidification) for these three cases are shown in figures 8a–c. These patterns are analysed on the basis of the following three criteria.

(1) Severity of segregation: The difference between maximum and the minimum composition in the entire cavity,
(2) areas under various segregation bands: These are computed from the solutal distribution fields.
(3) Global extent of segregation (GES): This is defined as the root mean square of the difference between the nodal composition and the mean composition (1 wt% C).

These quantities for various cases are listed in table 3. The GES for cases 1 and 2 are nearly the same though there are some minor differences in the areas under various segregation bands. The predominance of thermal buoyancy over solutal buoyancy in the case of iron–carbon alloy results in near identical GES for cases 1 and 2. Nevertheless, some minor differences in the magnitude of areas under various segregation bands are readily seen in table 3. Also, the comparison of macrosegregation patterns in figures 8a and b reveal that, compared to case 2, these patterns are more complex for case 1 near the hot wall.

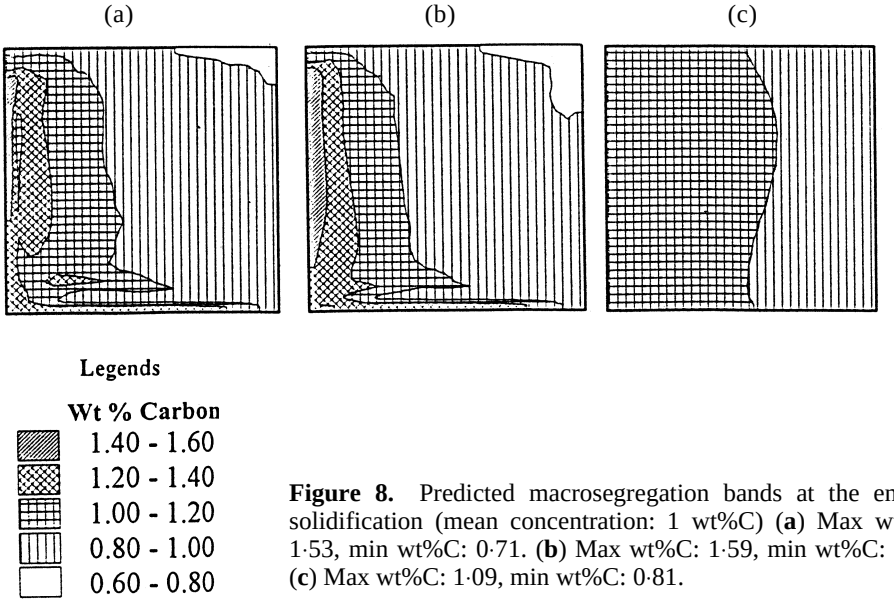

Figure 8. Predicted macrosegregation bands at the end of solidification (mean concentration: 1 wt%C) (**a**) Max wt%C: 1·53, min wt%C: 0·71. (**b**) Max wt%C: 1·59, min wt%C: 0·69. (**c**) Max wt%C: 1·09, min wt%C: 0·81.

In comparison to these two cases, the final macrosegregation profiles for case 3, shown in figure 8c, are very simple. Thus, the presence of single large vortex during the progress of solidification and decoupling of thermal and solutal fields in the mushy region result in simple macrosegregation profiles. The effect of better mixing in case 3 during the progress of solidification is reflected through the lower value of the severity of segregation. From table 3, it is seen that the severity of segregation for this case goes down to 27% as opposed to 84% and 90% for cases 1 and 2 respectively.

It is clear from the above discussion that the selection of appropriate auxiliary relationship requires great care as convection in the mushy region and the resultant macrosegregation depend on the choice of thermo-solutal coupling and selection of buoyancy generating forces. The numerical study presented above, clearly shows the effect of some of the critical assumptions on flow and macrosegregation during solidification of binary iron–carbon alloy. The following conclusions are drawn from the above study.

Table 3. Final macrosegregation for various cases.

	Final macrosegregation		Segregation band			
Various cases	Max.	Min.	< 0·8	0·8–1·2	> 1·2	GES
Case 1	1·53	0·71	1·13	76·26	22·60	17·16
Case 2	1·59	0·69	2·31	70·83	26·86	19·88
Case 3	1·09	0·81	0·00	100·0	0·0	6·53

- In evolution of macrosegregation, the role of solutal field in defining mush profile through thermo-solutal coupling is more important, compared to its effect through buoyancy forces.
- Solutal buoyancy plays important roles in the localised region: it is responsible for the reverse vortex near the hot wall and enhanced transport of solute along the hot wall of the cavities. These, in turn, cause complex macrosegregation patterns.
- Simplification in thermo-solutal coupling leads to major simplification in flow and macrosegregation patterns. Thus, it is undesirable to invoke such simplification in casting with slow or moderate rate of solidification.

These conclusions are exclusively for the iron–carbon system and would vary for other alloys.

5. Role of materials on double-diffusive convection

5.1 *Problem*

Material properties and equilibrium phase diagrams govern double-diffusive convection in a significant way. In this part of the paper, a critical study of the role of material properties alone on the double-diffusive convection is presented by simulating solidification of aqueous ammonium chloride, iron–carbon and lead–tin binary systems. Details of the mathematical model are presented elsewhere (Basu & Singh 1997).

Materials selected for the present study are Fe–C, Pb–Sn and NH_4Cl–H_2O. In all these three systems, the solute is lighter than the solvent and they all undergo eutectic reactions. The physical properties pertaining to these systems are listed in table 2. The corresponding dimensionless numbers are presented in the table 4. In this table, N signifies relative importance of solutal buoyancy with respect to thermal buoyancy in the mushy phase in the presence of solute rejection and is defined as

$$N = b_C / m b_T, \tag{8}$$

where, m is the slope of the liquidus.

Table 4. Dimensionless parameters.

	NH_4Cl–H_2O	Fe–C	Pb–Sn
Pr	7·49	0·17	$1{\cdot}87 \times 10^{-2}$
Da	$5{\cdot}0 \times 10^{-8}$	$2{\cdot}8 \times 10^{-9}$	$2{\cdot}8 \times 10^{-9}$
Ra_T	$1{\cdot}5 \times 10^{10}$	$9{\cdot}26 \times 10^{7}$	$1{\cdot}8 \times 10^{7}$
Ra_S	$7{\cdot}4 \times 10^{10}$	$8{\cdot}45 \times 10^{7}$	$8{\cdot}7 \times 10^{7}$
Le	7770·0	5740	27·7
Ste	25·0	0·554	0·262
Partition coeff., k	0·3	0·42	0·3
q/q_{FeC}	0·15	1·0	0·17
N	–14	–0·645	–1·4
P_d	6·526	0·6	0·3

In order to carry out a meaningful comparative study, initial conditions, namely superheat and concentration, and boundary condition, i.e., the imposed heat flux, are carefully chosen. The geometry of the cavity is the same for all the three materials. The initial composition for these systems is selected in such a way as to keep the ratio of initial composition to eutectic composition the same for all the three alloy systems. The initial superheat and imposed heat are chosen based on a similarity analysis.

Since the actual problem is governed by complex transport phenomena, simplifying assumptions need to be made to carry out the analyses. Assuming a lumped system with a heat flux imposed at the cold boundary (q), and liquid having certain initial superheat (ΔT), the following expression can be written based on the overall energy balance,

$$t = L r c \Delta T / q, \tag{9}$$

$$\mathrm{d}X/\mathrm{d}t = (q)/(r(\Delta H_f + c\Delta T). \tag{10}$$

Using (9) and (10), and satisfying similarity conditions in terms of equality of dX/dt and t between two materials systems, the following expressions for heat flux and superheat can be derived for any materials ('M') with respect to a reference material ('ref') and these are presented below,

$$\Delta T_M = \Delta T_{\mathrm{ref}}[\Delta H_M c_{\mathrm{ref}} / \Delta H_{\mathrm{ref}} c_M], \tag{11}$$

$$q_M = q_{\mathrm{ref}}(r \Delta H_M / r_{\mathrm{ref}} \Delta H_{\mathrm{ref}}). \tag{12}$$

For Fe–C, the imposed heat flux is assumed to be 60 kW/m^2 and the initial superheat and initial composition are taken as 5°C and 1 wt%, respectively. Assuming Fe–C as a reference system, the initial superheat and the heat flux for Pb–Sn and NH_4Cl–H_2O are calculated using (11) and (12) respectively. Similarly, the initial composition is calculated by keeping $C_{\mathrm{init}}/C_{\mathrm{eut}}$ the same for all three system. Thus, the initial temperature and composition for NH_4Cl–H_2O are 272·525°C and 18% respectively, whereas for Fe–C they are 1463°C and 1 wt% C respectively and for Pb–Sn, 292·25 and 15 wt% respectively. The boundary heat fluxes are obtained using (12).

It is important to note here that the selection of heat flux and superheat in this manner does not ensure constancy of overall rate of solidification and initiation of solidification for all the systems since the actual process is governed by a interaction of energy, solute and momentum transport. Nevertheless, the chosen basis does ensure that overall solidification rates as well as time for initiation of solidification are of the same order.

Figure 9 shows the progress of solidification for three binary alloy systems (Pb–Sn, Fe–C and NH_4Cl–H_2O). The progress of solidification is similar for metallic systems (Pb–Sn & Fe–C) but differs for the NH_4Cl–H_2O system. The reduction in superheat of melt ensures that solidification starts at the same time for all alloy systems. Figure 9 shows two curves for the NH_4Cl–H_2O solidification, NH_4Cl–H_2O(I) corresponds to modified heat flux after trial runs and NH_4Cl–H_2O(II) corresponds to heat flux obtained from similarity analysis.

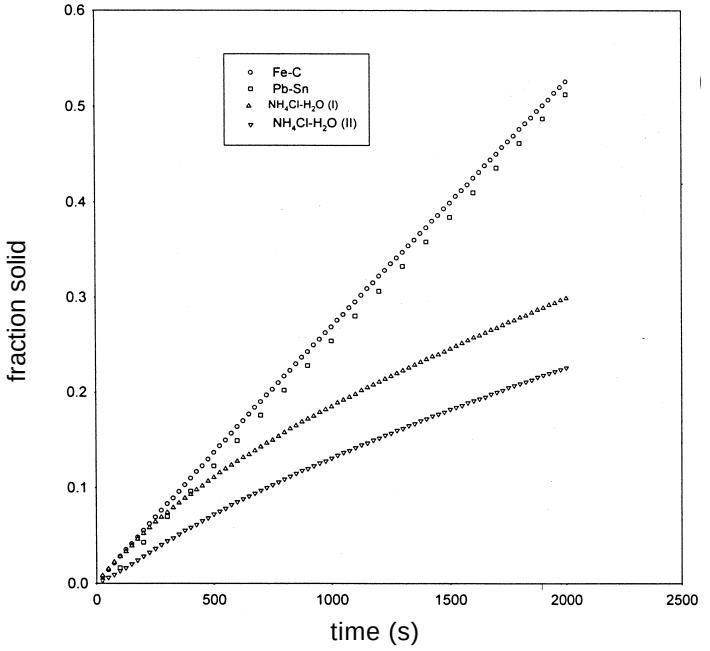

Figure 9. Progress of solidification. $NH_4Cl–H_2O$(I)-modified heat flux, $NH_4Cl–H_2O$(II)-heat flux obtained from similarity analysis.

Figure 10 shows the streamlines and macrosegregation at = 250, 500 and 2000 s, for the Fe–C system. At $t = 250$ s, the flow is essentially thermal buoyancy driven and anti-clockwise in nature. The flow in the mushy region is very weak and anti-clockwise in nature signifying thermal buoyancy driven flow. As for the macrosegregation, it is seen that there is depletion of solute along the cold wall and deposition of solute along the bottom of the cavity.

As solidification progresses, the flow field gradually shifts towards the hot wall of the cavity and weakens in strength due to spread of the mushy region in the cavity. This is evident from comparisons of flow fields at 500 and 2000 s. Macrosegregation gradually builds up with progress of solidification. The downward thermal-driven flow near the mushy region takes the solute with it and deposits it near the bottom and right vertical wall of the cavity. Similarly, the flow field leads to depletion of solute near the left vertical wall and top horizontal wall of the cavity. The dominance of thermal buoyancy over solutal buoyancy for Fe–C is observed which is due to $Ra_t/Ra_s > 1$ and $|N| < 1$. The resultant macrosegregation profile shows distinct trend where positive segregation is along the bottom and right wall of the cavity and negative segregation is along the cold wall and top wall of the cavity.

Figure 11 shows transient flow and macrosegregation fields at different times for the Pb–Sn system. As Pb–Sn has higher Ra_s, $Ra_t/Ra_s < 1$ and $|N| > 1$. So it is expected that the solutal buoyancy plays a significant role in convection. It can be seen from figure 11 that clockwise solutal-driven buoyancy vortex occupies most of the cavity at time = 250 s. This flow field results in higher solute concentrations at the top as seen in the macrosegregation

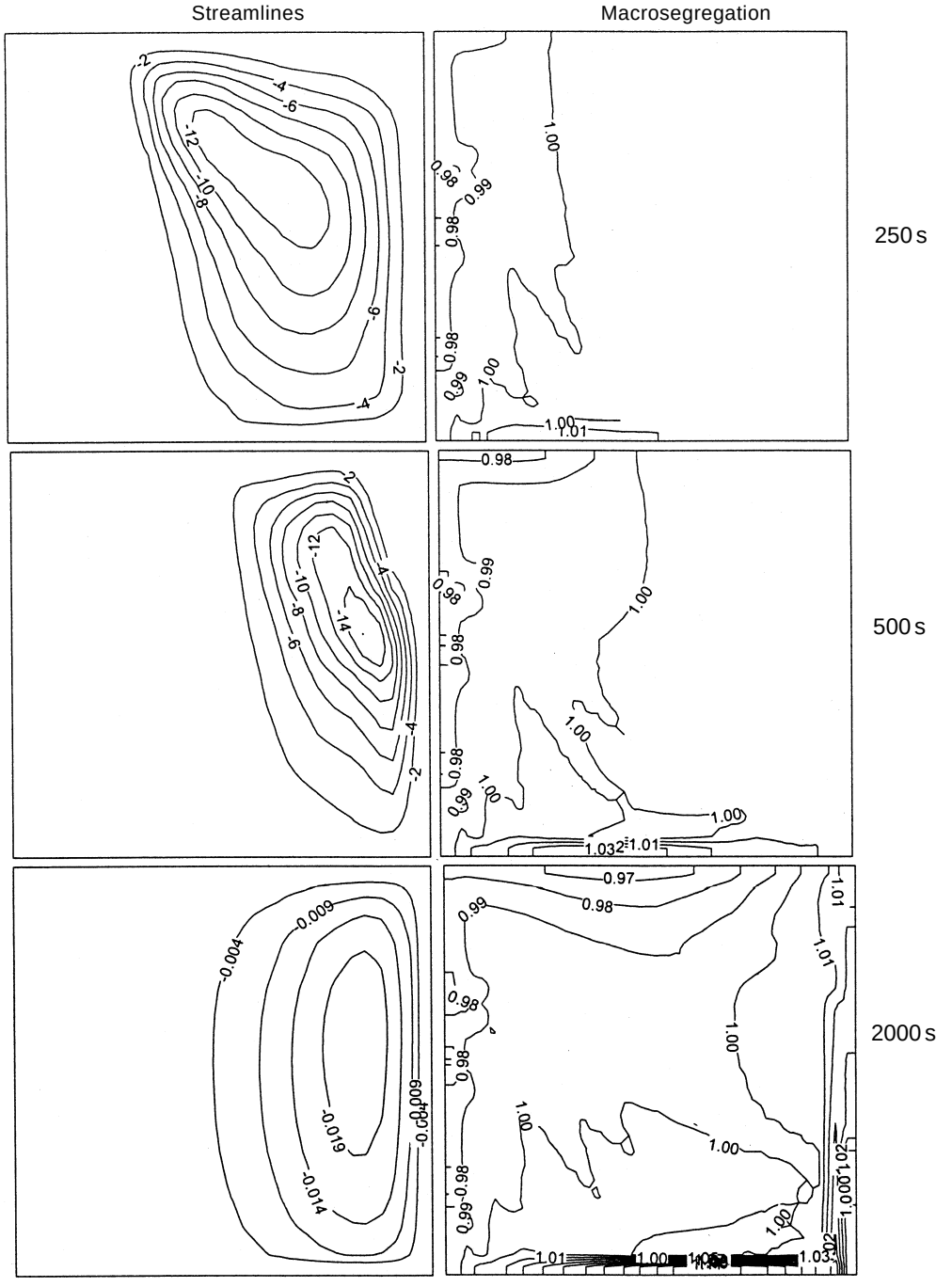

Figure 10. Streamlines and macrosegregation profile at t = 250, 500 and 2000 s (Fe–C).

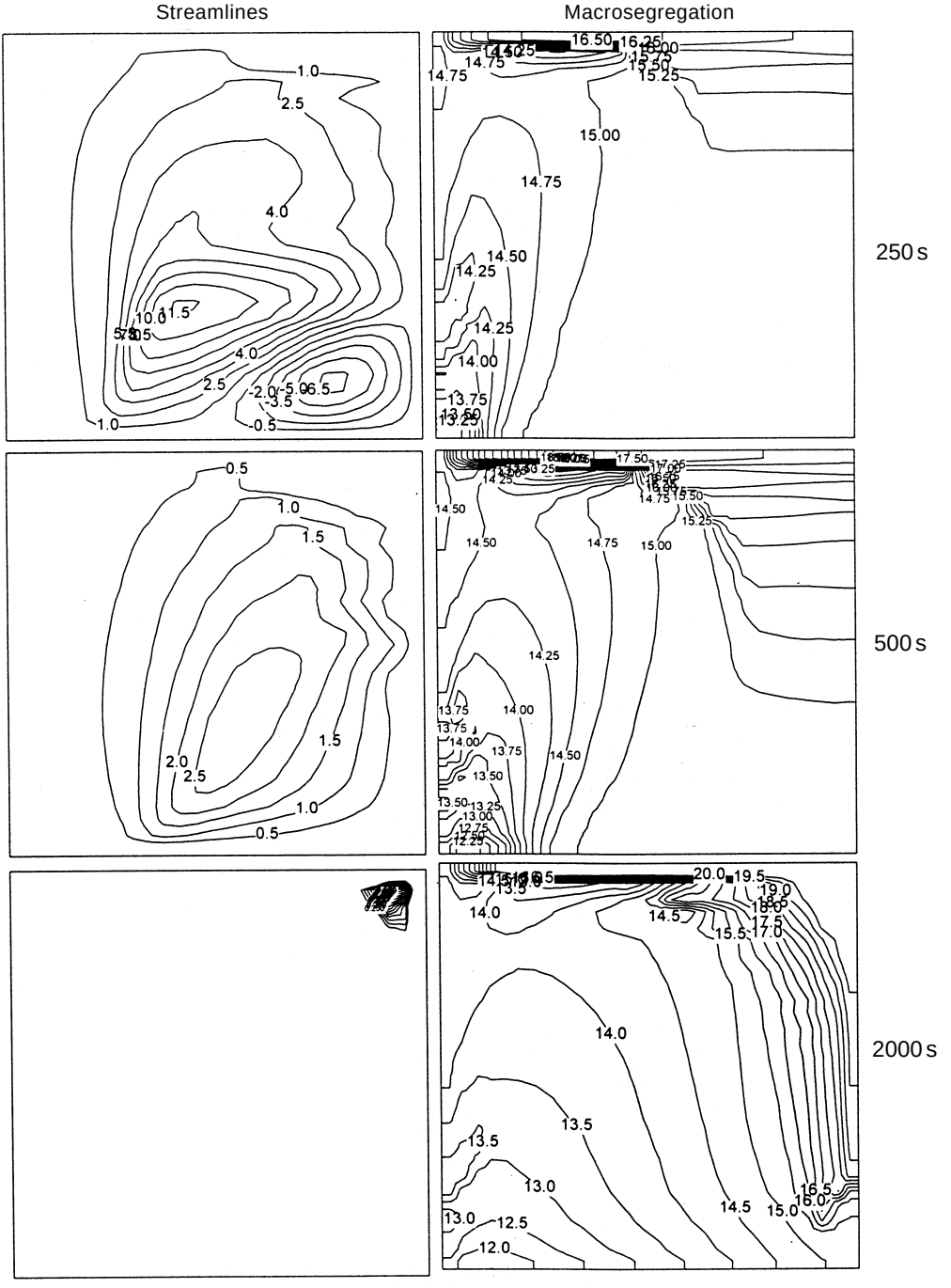

Figure 11. Streamlines and macrosegregation profiles at t = 250, 500 and 2000 s (Pb–Sn).

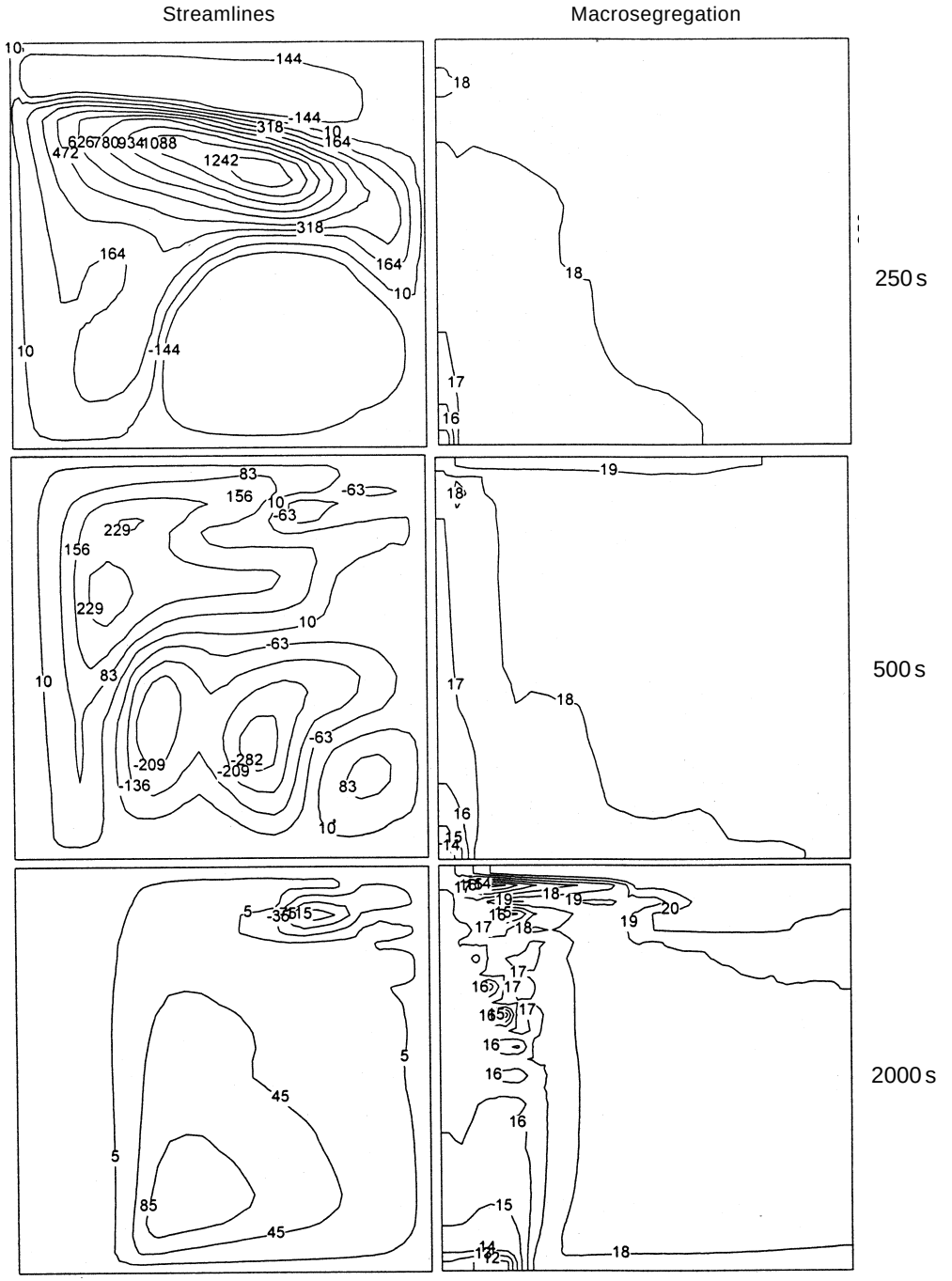

Figure 12. Streamlines and macrosegregation profiles at t = 250, 500 and 2000 s (NH_4Cl–H_2O).

pattern. As solidification progresses, the flow becomes very weak in the high solid region of the mushy zone ($f_s > 0{\cdot}5$). There is virtually no flow at $t = 2000$ s.

For the NH_4Cl–H_2O system (transient flow and microsegregation at different times, shown in figure 12), there are two vortices in the flow field at $t = 250$ s: the larger one is due to thermal buoyancy (anti-clockwise) and other near the solidification front is due to the solutal buoyancy (clockwise). For this system, $Ra_t/Ra_s < 1$ and $|N| \gg 1$. Thus, the dominance of solutal buoyancy over thermal buoyancy is readily seen near the cold wall. At 500 s, solutal buoyancy starts to play a major role and rejected solute gets transported out of the mush leading to enhanced solutal gradient in the bulk liquid. Due to strong flow, the fluid is well mixed in the cavity except in the mush. Due to high resistance to the flow in the mush, flow strength is very weak leading to vertical isotherms. As solidification progresses, solutal buoyancy completely dominates over the thermal one. Solute deposition is along the top and right walls of the cavity.

At time = 2000 s, it is seen that the effect of thermal buoyancy keeps on decreasing. Unlike in metallic systems, where the mush covers the entire cavity, the mushy region is thin in the case of the NH_4Cl–H_2O system and there is a completely solidified zone near the cold wall. It is also seen that the macrosegregation pattern near the cold wall becomes more pronounced by 2000 s.

The effect of material properties on double-diffusive convection and consequently on the macrosegregation is clearly evident from comparative study of three systems. The following conclusions are drawn from this work.

- In case of Fe–C, solutal buoyancy is weak compared to thermal buoyancy and the flow field is governed by thermal buoyancy. On the other hand, in Pb–Sn and NH_4Cl–H_2O systems, the flow is thermal buoyancy driven in the initial period of solidification but gradually transforms to solutal buoyancy driven flow.
- The nature of macrosegregation profile entirely follows the flow pattern. Thus in case of Fe–C the zone of positive segregation along the bottom and right vertical walls of the cavity. In contrast, the positive segregation zone for Pb–Sn and NH_4Cl–H_2O are along the top and right walls of the cavity.
- The segregation band is small in case of Fe–C owing to relatively small Raleigh numbers and high resistance to flow in the mush. On the other hand, in case of Pb–Sn and NH_4Cl–H_2O, the segregation bands are higher. In case Pb–Sn, Ra_s is higher compared to the Fe–C system and this is the driving mechanism for high segregation level. In comparison to these two, NH_4Cl–H_2O system has very high Ra_s and Ta_t but formation of a dense mushy region restricts macrosegregation to a level similar to Pb–Sn.

Thus, it is seen that the material properties affect the double-diffusive convection and consequent macrosegregation in a very significant way.

6. Summary and conclusions

The role of convection during solidification of binary alloys was investigated with the help of a mathematical model. The effect of various mush models on convection and consequent macrosegregation was examined. The predicted macrosegregation profiles

were compared with published experimental and numerical data. It was demonstrated that improvement in predictive power of the mathematical model is possible (in some parts) through selection of a better mush model. It was also observed that the anisotropic mush model shows better match with the experimental data. Subsequently, the importance of proper auxiliary relationship for thermo-solutal coupling in the mushy region was investigated through some careful numerical simulations. It was demonstrated that during the solidification of iron–carbon alloy, the role of solutal field in thermo-solutal coupling is more important compared to its contribution in buoyancy forces. It was observed that solutal buoyancy affects transport variables in localized regions. It was also shown that any relaxation in thermo-solutal coupling leads to major simplification in the flow and the macrosegregation patterns. Finally, the role of material parameters on double-diffusive convection was illustrated through comparative study of solidification of aqueous ammonium chloride, iron–carbon and lead–tin binary systems. It was shown that the nature of macrosegregation profile entirely follows flow patterns during the progress of solidification. Thus, in case of Fe–C, the zone of positive segregation is along the bottom and right vertical walls of the cavity. In contrast, the positive segregation zones for Pb–Sn and NH_4Cl–H_2O are along the top and right walls of the cavity. The role of buoyancy ratio (N), both magnitude and sign, during evolution of macrosegregation was demonstrated through comparative study.

This work was carried out under the Grant No. 1608-I by Indo-French Centre for the Promotion of Advanced Research, New Delhi. The authors thank Prof. E C Subbarao and Prof. A Ghosh for their critical remarks. The authors thank Prof. Mathai Joseph for providing support and encouragement.

List of symbols

c	specific heat (J/kg.K);
B	buoyancy term;
C	composition (wt%);
Da	Darcy number;
D	mass diffusion coefficient (m^2/s);
g	volume fraction or gravitational (m^2/s);
g_l	liquid fraction;
g_s	solid fraction;
h_f	enthalpy (J/kg);
ΔH	latent heat of fusion (J/kg);
H	cavity height (m);
k	thermal conductivity (W/m.K);
k_p	equilibrium partition coefficient;
K	permeability (m^2);
K_o	permeability coefficient (m^2);
Le	Lewis number;
N	stability number;

P pressure (N/m^2);
Pr Prandtl number;
P_d phase diagram coefficient;
q/q_{FeC} flux ratio;
Ra_S Raleigh number (solutal);
Ra_T Raleigh number (thermal);
S source term (W/m^3);
Ste Stefan number;
t time (s);
T_f fusion temperature (K);
u, v velocity component in x and y directions (m/s);
V velocity vector (m/s);
x, y orthogonal axes (m);
m dynamic viscosity (m^2/s);
r density (kg/m^3);
f general dependent variable.

Subscripts
c cold boundary;
e eutectic;
l liquid phase;
liq liquidus;
m mixture;
o initial condition;
s solid phase;
sol solidus.

References

Asai S, Muchi I 1978 Theoretical analysis and model experiments on the formation mechanism of channel type segregation. *Trans. ISIJ* 18: 90–98

Basu B 1991 A variable viscosity model to simulate fluid flow during alloy solidification with equiaxed growth. *Proc. 7th Int. Conference on Numerical Solutions for Thermal Problems*, Stanford University, USA, pp 131–145

Basu B, Singh A K 1997 Role and characterization of double-diffusive convection during solidification of binary alloys. *Proc. 3rd ISHMT-ASME Heat and Mass Transfer Conference and 14th National Heat and Mass Transfer Conference*, IIT, Kanpur, pp 129–161

Beckermann C, Viskanta R 1988 Double-diffusive convection during dendritic solidification of a binary alloy. *Phys. Chem. Hydrodyn.* 10: 195–210

Bennon W D, Incropera F P 1987 A continuum model for momentum, heat and species transporting binary solid–liquid phase change systems. *Int. J. Heat Mass Transfer* 30: 2161–2170

Brinkman H C 1947 A calculation of viscous force exerted by a fluid flowing on a dense swarm of particles. *Appl. Sci. Res.* A1: 81–86

Goyeau B, Benihaddadene T, Gobin D M, Quintard M 1999 Numerical calculation of permeability in a dendritic mushy zone. *Metall. Mater. Trans.* B30: 613–622

Ghosh A 1990 *Principles of secondary processing and casting of liquid steel* (New Delhi: Oxford and IBH) ch. 6, 7 and 9

Krane M J M, Incropera F P 1997 Experimental validation of continuum mixture model for binary alloy solidification. *J. Heat Transfer* 119: 783–791

Kurz W, Fisher D J 1992 *Fundamentals of solidification* 2nd edn. (Trans Tech Publication) pp 133–136

Patankar S V 1980 *Numerical heat transfer and fluid flow* (New York: McGraw-Hill)

Poirier D R 1987 Permeability for flow of liquid in columnar-dendritic alloys. *Met. Trans.* B18: 245–255

Scheil Z 1942 Bemerkunzen zur Schichtkristallbildung. *Z. Metallkunde* 34: 70–72

Singh A K, Basu B 1997 Mathematical modeling of macrosegregation of iron-carbon alloy: Effect of key process and physical parameters. *Proc. 3rd ISHMT-ASME Heat and Mass Transfer Conference and 14th National Heat and Mass Transfer Conference*, IIT, Kanpur, pp 925–930

Singh A K, Basu B 2000 On convection in mushy zone and its effect on macrosegregation. *Met. Trans.* A31: 1687–1692

Thompson M E, Szekely J 1988 Mathematical and physical modeling of double-diffusive convection of aqueous solutions crystallizing at a vertical wall. *J. Fluid Mech*. 187: 409–433

Voller V R, Prakash C 1987 A fixed grid modeling methodology for convection diffusion mushy region phase change problem. *Int. J. Heat Mass Transfer* 30: 1709–1719

West R 1985 On the permeability of the two-phase zone during solidification of alloys. *Met. Trans.* A16: 70

Worster M G 1997 Convection in mushy layers. *Annu. Rev. Fluid Mech*. 29: 91–122